Journal of CO_2 Utilization 41 (2020) 101290

Contents lists available at ScienceDirect

Journal of CO_2 Utilization

journal homepage: www.elsevier.com/locate/jcou

Identifying correlations in Fischer-Tropsch synthesis and CO_2 hydrogenation over Fe-based ZSM-5 catalysts

Renjie Liu[a], Zhiqiang Ma[a], Jeffrey D. Sears[b], Mitchell Juneau[a], Michael L. Neidig[b], Marc D. Porosoff[a,*]

[a] Department of Chemical Engineering, University of Rochester, Rochester, NY 14627, USA
[b] Department of Chemistry, University of Rochester, Rochester, NY 14627, USA

ARTICLE INFO

Keywords:
CO_2 hydrogenation
Fischer-Tropsch synthesis
Alkali promoters
ZSM-5
Tandem catalysts

ABSTRACT

Correlations in Fischer-Tropsch synthesis (FTS) and CO_2 hydrogenation are investigated over Fe supported on the acidic (H) and sodium (Na) forms of ZSM-5 (Si/Al = 50). FTS reactor studies indicate the selectivity toward olefins increases from 11% over Fe/H-ZSM-5 to 29.4% over Fe/Na-ZSM-5 because of Na increasing the surface basicity of the catalyst. Reactor studies are extended to CO_2 hydrogenation, where reverse water-gas shift is the dominant reaction, with Fe/Na-ZSM-5 displaying enhanced CO_2 adsorption, and in turn, higher CO selectivity (~80%) versus Fe/H-ZSM-5 (~60%). The catalysts are characterized by a variety of analytical techniques including Mössbauer spectroscopy, Fourier transform infrared (FTIR) spectroscopy and temperature programmed desorption (TPD) of NH_3 and CO_2 to correlate acid-base properties with catalytic performance. The findings of this study clearly show the selectivity of FTS and CO_2 hydrogenation can be attenuated toward the desired products by modifying the acid-base properties of the catalyst with sodium. These results are an important step toward designing high-performance catalysts for light olefin synthesis from CO and CO_2.

1. Introduction

As CO_2 levels in the atmosphere continue to increase, negative effects associated with climate change and ocean acidification require large-scale solutions. Catalytic conversion of CO_2 into value-added chemicals and fuels has attracted increasing attention [1–3], with specific emphasis on short-chain olefins for the production of plastics, polymers and specialty chemicals [4,5]. The high demand for lower olefins, ca. 200 million metric tons per year, makes them a valuable low-molecular weight target product with potential to sequester up to 23% of emitted CO_2 [6].

Currently, three main research directions have been proposed for catalytic conversion of CO_2 to olefins: (i) CO_2 conversion to methanol over a methanol synthesis catalyst, e.g. Cu-ZnO/Al_2O_3, followed by methanol-to-olefins (MTO) over a zeolite, e.g. SAPO-34 [7–13]; (ii) CO_2 conversion into CO via the reverse water-gas shift (RWGS) reaction, followed by Fischer-Tropsch synthesis to olefins (FTO) over Fe or Co-based catalysts [14–20]; and (iii) Direct hydrogenation of CO_2 to olefins over multi-functional, Fe or Co-based catalysts [21–25].

Direct hydrogenation of CO_2 to olefins (CO_2-FTO) is a very promising approach for industrial applications, however, controlling the selectivity is challenging. For example, Xie et al. have developed a tandem catalyst that combines RWGS and Fischer-Tropsch (FTS) over one well-defined nanostructure, which can directly convert CO_2 to C_2-C_4 hydrocarbons with a selectivity higher than 60% [26]. This core-shell tandem catalyst consists of Co impregnated onto a mesoporous silica shell, and a CeO_2 core decorated with Pt nanoparticles. During the CO_2 hydrogenation reaction, CO_2 is first reduced to CO via RWGS in the Pt/CeO_2 core, and subsequently converted to C_2-C_4 hydrocarbons via FTS over the Co/SiO_2 shell. Although the C_2-C_4 hydrocarbon selectivity is promising, the specific olefin selectivity is not reported.

Typically, Fe or Co-based catalysts are active for FTS, but when extended to CO_2, these catalysts produce CH_4 with high selectivity [27]. To tune these catalysts to produce olefins during CO_2 hydrogenation, research has focused on adding alkali metals to increase adsorption of the acidic CO_2 reactant and subsequently promote olefin selectivity. For example, Willauer et al. show that Fe-based catalysts promoted with potassium (K) produce olefins with increased selectivity, but the hydrocarbon products follow the Anderson-Shulz-Flory (ASF) distribution [28].

Controlling product distribution during CO_2-FTO typically requires the use of an acidic zeolite to control C-C coupling [29–35]. For

* Corresponding author.
E-mail address: marc.porosoff@rochester.edu (M.D. Porosoff).

https://doi.org/10.1016/j.jcou.2020.101290
Received 4 May 2020; Received in revised form 30 July 2020; Accepted 16 August 2020
Available online 29 August 2020

example, Wei et al. have physically mixed a Na-Fe_3O_4 active phase with a zeolite to synthesize a multifunctional catalyst for CO_2-FTO [36]. The authors show that three active sites catalyze the complex CO_2 hydrogenation reaction: Fe_3O_4 for RWGS, Fe_5C_2 for FTS, and acid sites (H-ZSM-5, H-BEA or H-MOR) for C-C coupling. Overall, H-ZSM-5 with Si/Al = 160 shows the highest selectivity (78%) to gasoline-range hydrocarbons (C_5-C_{11}), with low selectivity toward methane (4%). It is important to note that these values only include hydrocarbons, e.g. CO-free selectivity, and the selectivity to C_2-C_4 hydrocarbons (including olefins) is below 20% [36]. Nevertheless, this study demonstrates that a multifunctional catalyst can be a useful tool for controlling light olefin selectivity during direct CO_2 hydrogenation.

As shown above, Fe-zeolite tandem catalysts are promising, but because of their complexity, additional studies are required to understand the effect of zeolite properties, e.g. extra framework cations and Si/Al ratio, on catalytic performance for FTS and CO_2-FTO [37]. To elucidate these structure-property relationships, we synthesize Fe/Na-ZSM-5 and Fe/H-ZSM-5, characterize the catalysts with a variety of analytical techniques and evaluate reactor performance under typical FTS and CO_2 hydrogenation conditions. The findings of this paper demonstrate a correlation between acid-base properties and catalytic performance for each reaction, further advancing catalyst development for producing short-chain olefins from CO and CO_2.

2. Materials and methods

2.1. Materials

Tetraethyl orthosilicate (TEOS, 98%, Alfa Aesar), tetrapropylammonium hydroxide (TPAOH, 25 wt% in water, Acros Organics), aluminum nitrate nonahydrate ($Al(NO_3)_3{\cdot}9H_2O$, > 99%, Alfa Aesar), sodium hydroxide (NaOH, > 98%, extra pure, Alfa Aesar), ammonium nitrate (NH_4NO_3, 98%, Acros Organics), and iron (III) nitrate nonahydrate ($Fe(NO)_3{\cdot}9H_2O$, > 98%, Alfa Aesar) were used in this study without further purification.

2.2. Catalyst preparation

The ZSM-5 zeolites with Si/Al = 50 were synthesized via a hydrothermal synthesis method according to reports in the literature [38,39]. The proton and sodium forms of ZSM-5 were prepared by ion-exchange, and Fe was loaded by incipient wetness impregnation (5 wt% of Fe, metal basis) into each zeolite, resulting in Fe/H-ZSM-5 (Fe-H-M) and Fe/Na-ZSM-5 (Fe-Na-M). Additional catalyst synthesis details are found in the Supplementary Material.

2.3. Characterization of catalysts

X-ray diffraction (XRD) patterns were recorded on a Malvern Panalytical multi-purpose diffractometer over the range of 2θ = 5-70° at room temperature. N_2 physisorption was acquired on a Micromeritics ASAP 2020 analyzer at −196 °C. For physisorption experiments, all catalysts were degassed at 350 °C for 2 h under vacuum before analysis. Transmission electron microscopy (TEM) of the catalysts were performed in a FEI Tecnai G2-F20 scanning transmission electron microscope operated at an accelerating voltage of 200 kV. CO_2 pulse chemisorption experiments were performed in the AutoChem II analyzer, and the catalyst was pre-reduced at 450 °C under 10% H_2 in Ar before pulsing CO_2. Temperature-programmed desorption (TPD) measurements of CO_2, CO, H_2 and NH_3 were also performed on the Autochem II. The pretreatment conditions were the same as pulse chemisorption. After adsorption of the probe molecule, the sample was purged with helium and heated at a rate of 4 °C/min to 650 °C.

Pyridine adsorption infrared spectroscopy was applied to determine the relative concentration of Brønsted and Lewis acid sites in the catalysts with a Nicolet iS50 Fourier transform infrared (FTIR) spectrometer (Thermo Scientific) equipped with a MCT/A detector. Approximately 50 mg of catalyst was loaded into a reactor cell (Harrick Praying Mantis™ diffuse reflection with ZnSe window). After degassing the catalyst, pyridine was introduced into the cell by bubbling N_2 through liquid pyridine. Subsequently, the cell was purged with Ar to remove the physically adsorbed pyridine. The relative concentration of Brønsted and Lewis acid sites (B/L ratio) was calculated from the integrated IR bands at 1550 and 1450 cm^{-1}, respectively. Additional catalyst characterization details for each analytical technique are found in the Supplementary material.

Mössbauer spectroscopy was used to characterize the iron phases pre- and post-FTS. All solid samples for ^{57}Fe Mössbauer spectroscopy were run on nonenriched samples. All samples were prepared in Delrin Mössbauer sample cups under ambient conditions and subsequently frozen in liquid N_2. Samples were fitted with an inner Delrin cup prior to freezing. Low temperature ^{57}Fe Mössbauer measurements were performed using a SeeCo. MS4 Mössbauer spectrometer integrated with a Janis SVT-400 T He/N_2 cryostat for measurements at 80 K. Isomer shifts were determined relative to α-Fe at 298 K. All Mössbauer spectra were fit using the program WMoss (SeeCo). All Mössbauer spectra display the raw data (black dots) and where applicable, the total fit (black line) and individual components represented by colored two-line and six-line hyperfine patterns. Errors of the fit analyses are $\delta \pm 0.02$ mm/s and $\Delta E_Q \pm 3\%$. For multicomponent fits, the quantitation errors of individual components were ± 3%. Note the following abbreviations: Full width at half maximum (FWHM), Isomer Shift (δ), Electric Quadrupole Splitting (ΔE_Q), and Internal Magnetic Field (H(int)).

2.4. Reactor studies

For typical FTS and CO_2 hydrogenation reactor studies, 200 mg of catalyst was loaded into the reactor and reduced under 40 mL/min H_2 for 2 h at 450 °C and 50 psig. After reduction, the reactor was switched to the bypass loop and pressurized to 300 psig with the reactant gas mixture. For CO_2 hydrogenation, the gas composition was 10 mL/min CO_2, 30 mL/min H_2 and 5 mL/min Ar. For Fischer-Tropsch synthesis, the gas composition was 10 mL/min CO, 20 mL/min H_2 and 15 mL/min Ar to achieve H_2:CO_x ratios of 3:1 or 2:1, respectively. The concentration of gases exiting the reactor were evaluated with an in-line Agilent gas chromatograph. The reactions were determined to be free of mass-transfer limitations, as determined by the Koros-Nowak criterion in Fig. S1 of the SI [40].

2.5. In situ FTIR reactor studies

In situ FTIR reactor studies were conducted to characterize adsorption behavior of reactants and identify reaction intermediates with the FTIR spectrometer stated above. Approximately 50 mg of catalyst was loaded into the cell and reduced at 450 °C for 2 h followed by introducing the probe gases for 15 min. For CO adsorption, the gas composition was 3.5 mL/min CO and 3.5 mL/min Ar to achieve CO/Ar ratio of 1:1. For Fischer-Tropsch synthesis, the gas composition was 3.5 mL/min CO, 7 mL/min H_2 and 21 mL/min Ar to achieve CO:H_2:Ar ratios of 1:2:6. Then, spectra were recorded under vacuum.

3. Results and discussion

All catalysts are confirmed to have a typical MFI topology with high crystallinity according to XRD patterns and N_2 physisorption isotherms (Fig. S2 and S3 of the Supplementary material). Two weak peaks at 2θ = 33 and 36° in the XRD patterns match the Fe_2O_3 hematite phase of Fe oxide. The catalysts exhibit similar microporous adsorption-desorption behaviors (type I), and hysteresis loops at high relative pressure are present, which are due to mesopores [41,42]. After introduction of the Fe species, the BET surface area, total pore volume and micropore volume are relatively unchanged, as shown in Table 1.

Table 1
N_2 physisorption, CO and CO_2 chemisorption results over the parent H-ZSM-5, Fe-H-M and Fe-Na-M catalysts.

Catalyst	S_{BET} (m^2/g)	S_{micro} (m^2/g)	V_{total} (cm^3/g)	V_{micro} (cm^3/g)	Total (μmol NH_3/g)	B/L ratio	CO uptake (μmol/g STP)	CO_2 uptake (μmol/g STP)	Average diameter[1] (nm)	Average diameter[2] (nm)
H-ZSM-5	325	161	0.55	0.12	350	1.06	0	0	N/A	N/A
Fe-H-M	345	166	0.66	0.12	270	0.06	12.1	87.1	19.6(17.5) ± 9.5	29.6
Fe-Na-M	338	180	0.63	0.13	260	0.01	1.3	232.6	18.2(16.2) ± 8.4	33.3

[1]Mean particle size calculated from TEM measurements, with median particle diameters in parenthesis.
[2]Average diameter estimated by performing Scherrer analysis using the (104) reflection of Fe_2O_3 at $2\theta = 33.1°$[43].

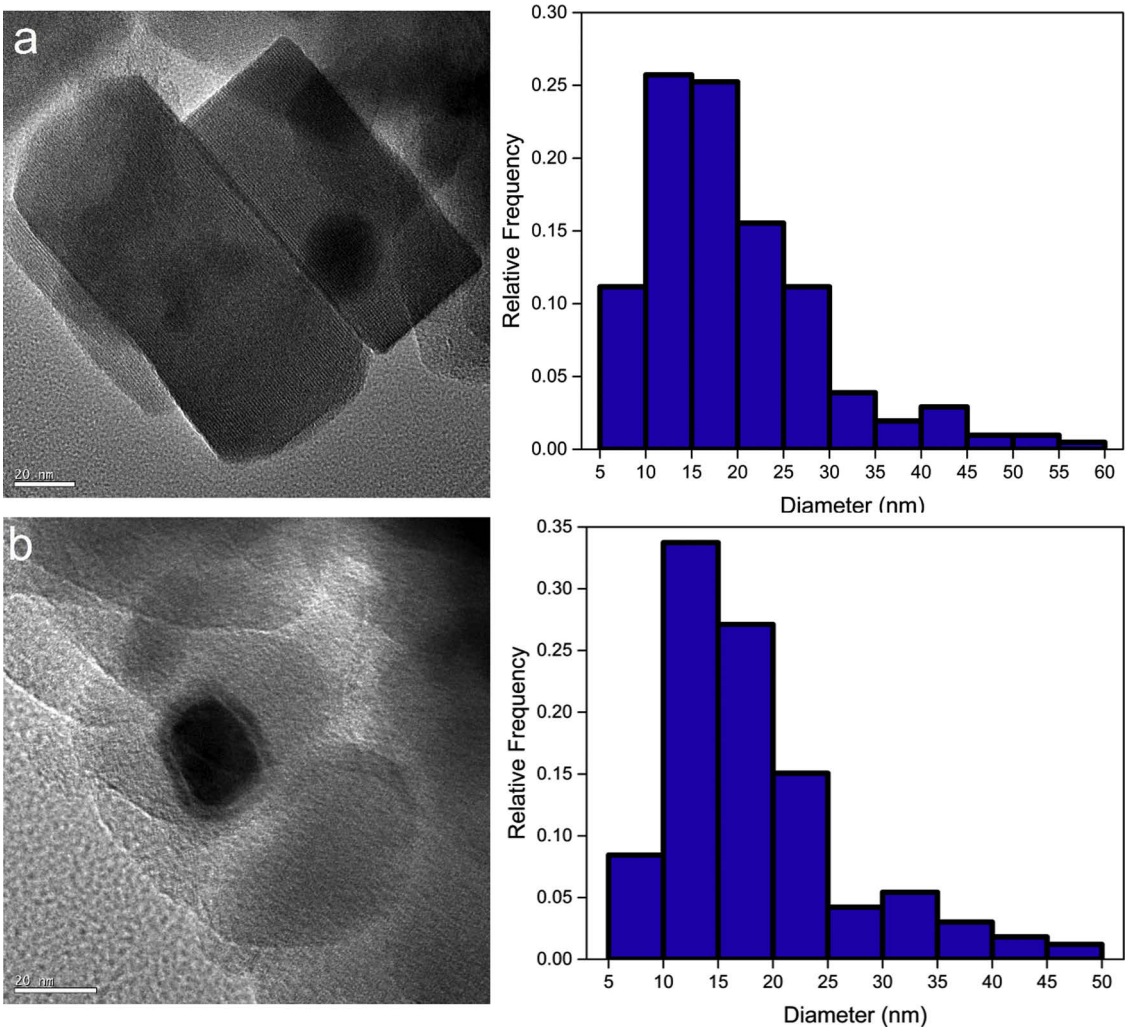

Fig. 1. TEM images with corresponding histograms of particle size distributions of (a) Fe-H-M and (b) Fe-Na-M. All samples are reduced under 40 sccm H_2 for 2 h at 450 °C and 50 psig prior to inserting in the TEM.

These physical properties are consistent with TEM images of the catalysts in Fig. 1, which includes the particle size distributions of both catalysts. Particle size distributions in Table 1 are calculated by measuring horizontal particle diameters in several different images of both Fe/ZSM-5 catalysts. Median particle size is found to be 16.2 nm and 17.5 nm for Fe-Na-M and Fe-H-M, respectively. For Fe-H-M, multiple larger and smaller particles are also observed in Fig. S4 and S5, resulting in the wider standard deviation in particle size.

To confirm if the particle size results in differences in the number of active sites, CO and CO_2 uptake values are also included in Table 1. Fe-H-M shows nine times higher CO uptake (12.1 μmol/g) than Fe-Na-M (1.3 μmol/g). However, for CO_2 uptake, the opposite trend is observed. Fe-Na-M has higher CO_2 uptake than that of Fe-H-M, which are 232.6 and 87.1 μmol/g, respectively. The significant difference in CO and CO_2 adsorption over the Fe-based catalysts is likely caused by the presence of Na, which increases the surface basicity of Fe-Na-M relative to Fe-H-M, resulting higher uptake of the acidic CO_2 molecule [44–46] and a ten-fold decrease in adsorption of the slightly basic CO molecule [47]. Similar conclusions have been reported by An et al., who use CO_2-TPD to conclude K and Na increase the surface basicity of Fe/SiO_2 for FTS [45].

The effect of CO and CO_2 adsorption on FTS reactor performance can be observed in Table 2. For Fe-H-M, which adsorbs a greater amount of CO, the catalyst exhibits higher CO conversion than Fe-Na-M, while selectivities to CH_4 and CO_2 increase with increasing temperature, suggesting high temperature favors methanation and water-gas shift. There is also an observed increase in olefin production with increasing temperature over both catalysts [48–50]. Relative to Fe-H-M,

Table 2
Summary of catalytic performance of Fe-based catalysts for FTS.

Catalyst	Temperature (°C)	CO Conversion (%)	Selectivity (%)[a]					Olefin yield (mL/h/g_{cat})	α value[d]	Carbon balance (%)
			CH_4 (%)	CO_2 (%)	C_2-C_4 hydrocarbons (%)[b]	C_2-C_4 olefins (%)	Other (%)[c]			
Fe-H-M	300	14.4	36.8	21.3	30.2	6.2	11.7	26.8	0.37	95.0
	320	17.4	39.2	19.0	30.9	8.8	10.9	45.9	0.31	95.3
	335	21.8	40.4	22.6	24.3	11.0	12.7	71.9	0.31	91.8
	350	24.7	42.1	26.4	23.2	10.6	8.3	78.5	0.31	94.9
Fe-Na-M	300	7.3	47.8	12.9	27.8	20.3	11.5	44.5	0.23	97.0
	320	9.5	38.5	16.5	33.9	26.9	11.1	76.7	0.33	98.2
	335	12.1	31.3	19.0	39.1	29.4	10.6	106.7	0.40	97.4
	350	16.3	26.6	22.1	36.9	26.6	14.4	130.1	0.35	92.6

Data are reported at 12 h of time-on-stream (TOS). Reaction conditions: $CO:H_2$ = 1:2, CO (10 mL/min), H_2 (20 mL/min), and Ar (15 mL/min) as balance gas and internal standard; P = 300 psig, 200 mg catalyst, GHSV = 13500 mL h^{-1} g_{cat}^{-1}. Na or H: Na or H form zeolite. A: Molar carbon-based selectivity including CO_2; b: Molar carbon-based selectivity of C_2-C_4 hydrocarbons (C_2-C_4 olefins included); c: Molar carbon-based selectivity of other products, including long-chain (C_5+) hydrocarbons, oxygenated and unknown products; d: α value is the hydrocarbon chain growth probability, calculated based on the Anderson-Schulz-Flory (ASF) distribution model.

FTS over Fe-Na-M results in slightly suppressed CO_2 selectivity, which is consistent with the higher CO_2 uptake over Fe-Na-M. Methane selectivity also decreases with increasing temperature, while the selectivity for C_2-C_4 hydrocarbons, especially C_2-C_4 olefins increases significantly, which is correlated with the Na promoter decreasing the concentration of acid sites [51–58]. The effect of Na loading on FTS is shown in Table S1, where CO conversion increases up to 1 wt% Na, followed by decreasing CO conversion from 1 to 3 wt% Na. At a Na loading of 3 wt%, the olefin selectivity is at a maximum of 27.8%, while the CH_4 selectivity monotonically decreases with Na loading. These results agree with previous literature reports on Na promoters for Fe-based catalysts [51].

Because the acid-base properties of the Fe-based catalysts appear to influence the selectivity, NH_3 adsorption and pyridine FTIR are used to measure total acidity and type of acid sites, shown in Table 1 and Fig. 2. As seen in the data, the total acidity of the parent H-ZSM-5 is 0.35 mmol/g and decreases to 0.27 mmol/g and 0.26 mmol/g for Fe-H-M and Fe-Na-M, respectively. These findings agree with those of Xu et al., who show the addition of 10 wt% Fe to H-ZSM-5 decreases the total acidity by 27% (from 0.61 to 0.44 mmol/g), which is similar to the value reported here (~23% decrease from 0.35 to 0.27 mmol/g) [50].

As for the type of acid sites, the results of pyridine FTIR in Table 1 and Fig. 2 indicate that the relative Brønsted to Lewis acid ratio (B/L ratio) of the parent H-ZSM-5 is 1.06, while after introduction of Fe, the B/L ratio decreases to 0.06 for Fe-H-M and 0.01 for Fe-Na-M. For Fe-H-M, the significant decrease of the B/L ratio is attributed to selective adsorption of the Fe species onto Brønsted acid sites [59,60], while the parent Na-ZSM-5 does not contain Brønsted acid sites (extra framework protons) after synthesis. Together, these results suggest that the total acidity, measured by NH_3 adsorption, does not strongly influence the production of light olefins, while decreasing Brønsted acid site concentration from substituting extra framework Na cations increases olefin selectivity.

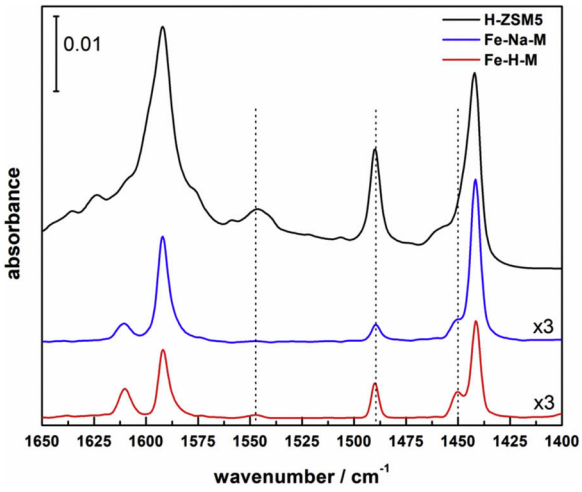

Fig. 2. Pyridine FTIR spectra of the Fe-H-M and Fe-Na-M catalysts with H-ZSM-5 included as a reference. Peaks at ca. 1550 cm^{-1}, 1490 cm^{-1} and 1450 cm^{-1} correspond to Brønsted, complexes of Brønsted and Lewis, and Lewis acid sites, respectively.

To further characterize the acidic properties of the Fe-ZSM-5 catalysts, NH_3 and CO_2-TPD measurements are shown in Fig. 3 (CO-TPD profiles are in Fig. S6 of the Supplementary Material). For NH_3-TPD of the parent H-ZSM-5, two desorption peaks are observed at 175 °C and 340 °C, which are ascribed to weak and strong acid sites, respectively [61,62]. After introduction of Fe into H-ZSM-5, the peak at 175 °C remains unchanged, but the peak at 340 °C shifts to a higher temperature of 460 °C over the Fe-H-M catalyst [63]. Similar to our observations, Lima et al. show that the addition of Fe to ZSM-5 also does not change the NH_3 desorption temperature of weak acid sites, but shifts the desorption temperature of strong acid sites from 388 °C to 448 °C [63].

For Fe-Na-M, the peak at high temperature peak disappears, suggesting strong acid sites are not present in this catalyst, which agrees with the pyridine FTIR in Fig. 2, and the low temperature peak corresponding to weak acid sites becomes broader. These findings are consistent with those of Putluru et al., who show that alkali promoters preferentially bind to the strong acid sites of zeolites, decreasing their concentration, while weak acid sites are only slightly affected [64].

For basic site characterization by CO_2-TPD (Fig. 3b), the maximum desorption peaks for CO_2 over both catalysts are similar (~175 °C), however, the total amount of adsorbed CO_2 is significantly less over Fe-H-M (87.1 μmol/g), relative to Fe-Na-M (232.6 μmol/g), as shown in Table 1. This is due to Na increasing the surface basicity, thus resulting in a greater extent of CO_2 adsorption, which is correlated with lower CO_2 selectivity during FTS.

To gain insight into the active sites for FTS over the Fe-based catalysts, we have employed a combination of H_2-TPR, diffuse reflectance FTIR and Mössbauer spectroscopy. The H_2-TPR profiles in Fig. S6 give some insight into the phase of the reduced catalysts, indicated by two reduction steps at an intermediate temperature region of 350–500 °C and a high temperature region of 500-700 °C. These steps correspond to the reduction of Fe^{3+} to Fe^{2+} and Fe^{2+} to Fe°, respectively. In both catalysts, the main reduction peak is located at ~400 °C, which is the reduction of isolated Fe^{3+} to Fe^{2+}, such as Fe^{3+} in Brønsted acid sites and/or small Fe clusters [64–66]. This suggests the bulk of the catalyst is not fully reduced before reaction, consistent with the XRD showing

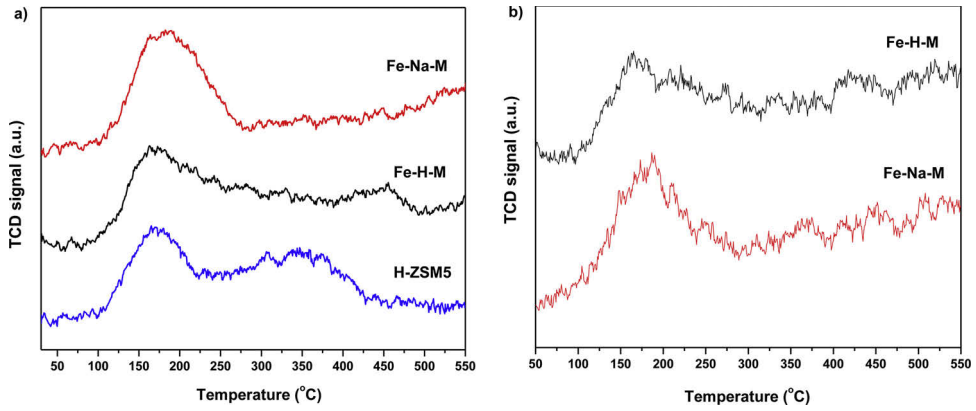

Fig. 3. Temperature program desorption profiles of the Fe-H-M and Fe-Na-M catalysts. (a) NH_3-TPD; and (b) CO_2-TPD.

evidence of Fe_2O_3 prior to reduction. Unlike Fe-H-M, the presence of Na in Fe-Na-M broadens the intermediate reduction temperature. Furthermore, the complex TPR profiles also suggest that multiple Fe species exist within the catalysts, but Fe^{3+} is predominant [64].

Further evidence on the structure of the reduced catalyst is shown via FTIR of adsorbed CO in Fig. 4. For both catalysts, the peaks at 2064 cm^{-1} and 2058 cm^{-1} are assigned to linearly adsorbed CO on partly reduced Fe^{2+} particles. The incomplete reduction of Fe, which agrees with the H_2-TPR in Fig. S6a, increases the electron donating capacity of Fe^{2+} and shifts the vibrational frequency of linearly adsorbed CO to a lower wavenumber, when compared to Fe^{2+} deposited on a flat surface (2155 cm^{-1}) [67–69]. The shoulder at 2050 cm^{-1} corresponds to CO linearly adsorbed on Fe° interacting with carbon and/or oxygen atoms [67,70] while the peak at 1933 cm^{-1} is due to bridged CO on flat metallic Fe [70,71]. Additionally, the IR band at 1800 cm^{-1} is ascribed to inclined bridged CO adsorbed on Fe° (111) shallow hollow sites [72].

The relative integrated area of the bands from 2064 cm^{-1} to 2058 cm^{-1} are greater over Fe-Na-M, which agree with the CO-TPD profiles in Fig. S6b, further suggesting a larger amount of CO is adsorbed over Fe-Na-M. It is also worth noting that Fe-H-M contains a unique feature at 1734 cm^{-1}, representing CO adsorbed on 4-fold deep hollow Fe(100) sites [73].

For studying the structure of the Fe-based catalysts, ^{57}Fe Mössbauer spectroscopy was used to identify the iron species present in the as-prepared and post-FTS Fe-Na-M and Fe-H-M catalysts [74]. As shown in Fig. 5, iron oxide species are found in both Fe-Na-M and Fe-H-M prior to FTS, which is consistent with XRD. Following FTS, numerous iron carbide species are found in both samples, with Fe-Na-M containing a larger fraction of Fe carbide relative to Fe-H-M as shown in Table. S2

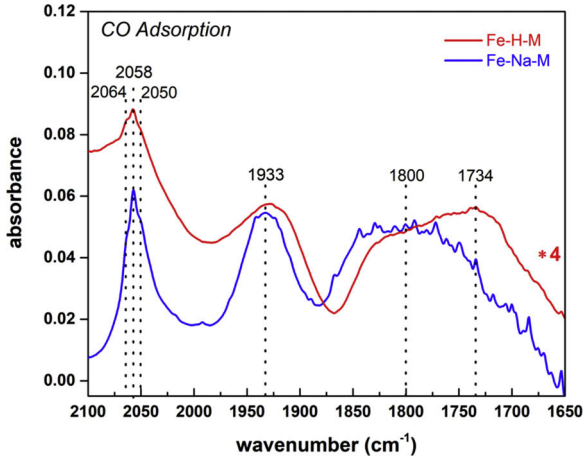

Fig. 4. FTIR spectra of CO adsorbed on reduced Fe/ZSM-5 catalysts.

(88% vs 78%, respectively). More specifically, Fe-Na-M also contains a higher fraction of Fe_5C_2 (58% vs 47%), the active phase for FT to olefins [75], suggesting the Mössbauer findings are consistent with the FTS reactor data.

Insight into the catalytic mechanism is shown in Fig. 6 for the FTIR of adsorbed intermediates during *in situ* FTS. The band at 3740 cm^{-1} is assigned to hydroxyl groups adsorbed over Fe-H-M and Fe-Na-M. Fe-H-M has a significantly larger amount of adsorbed hydroxyl groups when compared to Fe-Na-M due to the Brønsted acid sites present in H-ZSM-5 [76]. Gaseous CO_2 is present in the range of 2400–2300 cm^{-1}, as expected, and peaks describing chemically bonded CO are observed within the same range as discussed for CO-FTIR in Fig. 4. However, the band at 1734 cm^{-1}, corresponding to CO adsorbed on 4-fold hollow sites on Fe° (100), is no longer present after FTS in Fig. 6. Merill et al. have demonstrated that CO adsorption over 4-fold hollow sites on Fe (100) can be hindered by hydrogen atoms, which may explain why the band at 1734 cm^{-1} disappears during FTS [73,77]. Additionally, two characteristic peaks of carbonate species are found at 1240 cm^{-1} and 1168 cm^{-1} [70,73,76].

The close-up view of the 3100–2700 cm^{-1} region, representing hydrocarbon species in Fig. 6b indicates gaseous methane is present, which is assigned to the band centered at 3011 cm^{-1} [73,78,79]. The bands at 2955 cm^{-1} and 2935 cm^{-1} are ascribed to the asymmetric CH stretching modes of methyl -CH_3 and methylene -CH_2, respectively, while the corresponding symmetric stretching modes are at 2871 cm^{-1} and 2856 cm^{-1} [73,79]. The presence of increased hydrocarbon species on the surface of Fe-H-M is consistent with coking leading to the rapid deactivation observed in Fig. 7 and XPS data of the C1s electron showing increased coking of the Fe-H-M catalyst relative to Fe-Na-M in Fig. S7.

To further study deactivation, we evaluated our catalysts for 48 h time-on-stream during FTS, as shown in Fig. 7. For Fe-H-M (Fig. 7a), the conversion decreases from 24.9 to 14.4%, indicating slight deactivation. For Fe-Na-M (Fig. 7b), the conversion first increases from 13.2 to 15.0% and then decreases to 11.1% after 48 h time-on-stream, indicating largely improved stability over Fe-H-M. Furthermore, the induction period over the first ~10 h time-on-stream is consistent with Mössbauer results, suggesting the formation of a Fe_5C_2 phase. Our observations of improved stability over Fe-Na-M are consistent with previous studies showing Na results in increased olefin yield and stability of to Fe/ZSM-5 catalysts [80].

The deactivation could be due to a combination of factors including sintering and phase transformation of the Fe species [80–82], coke formation [83–86] and water poisoning [87]. To gain some insight into the cause of the deactivation, XRD patterns and textual properties of the spent catalysts are found in Fig. S8 and Table S3 of the Supplementary material. According to XRD in Fig. S8, the structure of the ZSM-5 in the spent catalysts (Fe-H-M and Fe-Na-M) is preserved and the weak peaks

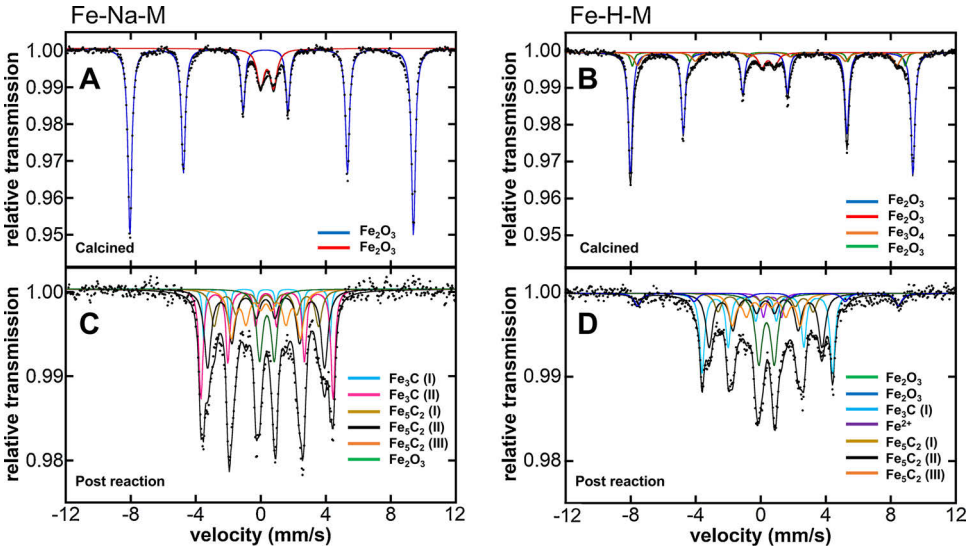

Fig. 5. 80 K ^{57}Fe Mössbauer spectra of as-prepared (A) Fe-Na-M, (B) Fe-H-M and post-FTS (C) Fe-Na-M and (D) Fe-H-M. For a compilation of all multicomponent fitted Mössbauer parameters see Table S2.

at 2θ = 33 and 36° associated with Fe_2O_3 disappear, consistent with formation of Fe carbides that are observed in Mössbauer spectroscopy. Although the surface area and pore volume of Fe-H-M remains relatively constant in Table S3, there is a marked decrease observed over Fe-Na-M. These findings together with the C1s XPS in Fig. S7, suggest that coke formation is a possible mechanism of deactivation, but the significant loss of surface observed over Fe-Na-M is likely due to the formation of the additional low surface area Fe carbide phases observed in Mössbauer.

After completing FTS studies, we are interested in determining if any trends observed in FTS from the addition of Na can be correlated with CO_2 hydrogenation. As previously mentioned, highly active FTS catalysts are typically methanation catalysts during CO_2 hydrogenation, but as shown in the CO_2 hydrogenation results in Table 3, CO produced via RWGS is the primary product over both catalysts. This is apparent for Fe-Na-M, where CO selectivity is over 80%, consistent with previous

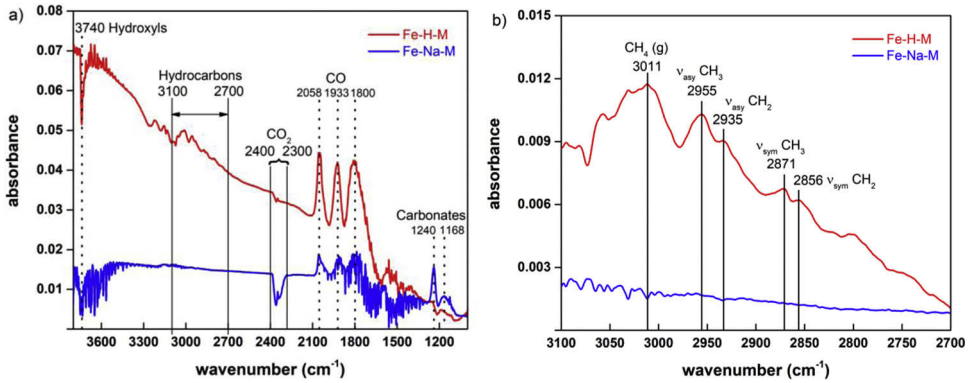

Fig. 6. (a) FTIR spectra of adsorbed species of FTS over reduced Fe/ZSM-5 catalysts, with (b) close up view of 3100–2700 cm^{-1} region.

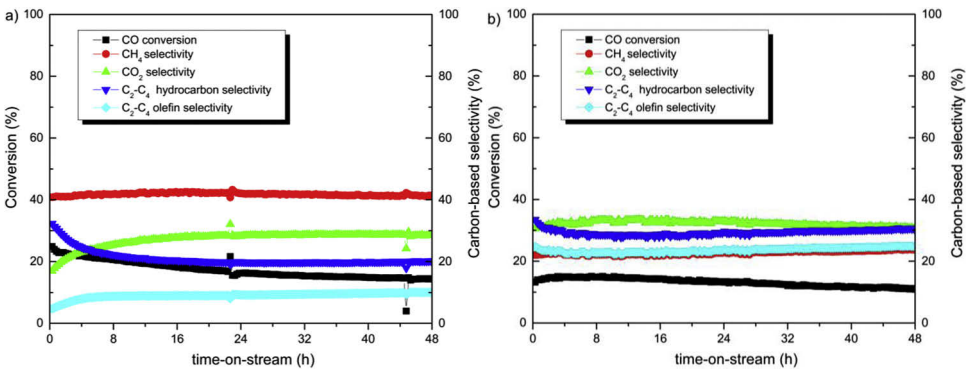

Fig. 7. Reactor performance versus time-on-stream for (a) Fe-H-M and (b) Fe-Na-M during FTS. Reaction conditions: CO:H_2 = 1:2, CO (10 mL/min), H_2 (20 mL/min), and Ar (15 mL/min) as balance gas and internal standard; T = 350 °C, P = 300 psig, 200 mg catalyst, GHSV = 13500 mL h^{-1} g_{cat}^{-1}.

Table 3
Summary of catalytic performance of Fe-based catalysts for CO_2 hydrogenation.

Catalyst	Temperature (°C)	CO_2 Conversion (%)	Selectivity (%)[a]					Olefins yield (mL/h/g_{cat})	α value[d]	Carbon balance (%)
			CH_4 (%)	CO (%)	C_2-C_4 hydrocarbons (%)[b]	C_2-C_4 olefins (%)	Other (%)[c]			
Fe-H-M	300	3.4	27.8	58.3	12.2	0.4	1.7	0.4	0.30	98.9
	320	4.6	28.6	58.9	11.1	0.4	1.4	0.6	0.29	98.5
	335	5.7	28.4	60.9	9.7	0.4	1.0	0.7	0.24	98.4
	350	6.8	26.9	64.3	8.1	0.1	0.7	0.2	0.23	98.2
Fe-Na-M	300	1.7	16.2	80.0	3.8	0	0	0.0	0.17	100
	320	2.7	14.3	81.9	3.7	0.3	0.1	0.2	0.16	99.1
	335	3.8	13.5	83.8	1.4	0.3	1.3	0.3	0.17	98.3
	350	5.9	17.6	76.4	3.1	1.0	2.9	1.8	0.11	98.0

Data are reported at 12 h time-on-stream (TOS). Reaction conditions: CO_2:H_2 = 1:3, CO_2 (10 mL/min), H_2 (30 mL/min), and Ar (5 mL/min) as balance gas and internal standard; P = 300 psig, 200 mg catalyst, GHSV = 13500 mL h^{-1} g_{cat}^{-1}. Na or H: Na or H form zeolite. a: Molar carbon-based selectivity including CO; b: Molar carbon-based selectivity of C_2-C_4 hydrocarbons (C_2-C_4 olefins included); c: Molar carbon-based selectivity of other products, including long-chain (C_5+) hydrocarbons, oxygenated and unknown products; d: α value is the hydrocarbon chain growth probability, calculated based on the Anderson-Schulz-Flory (ASF) distribution model.

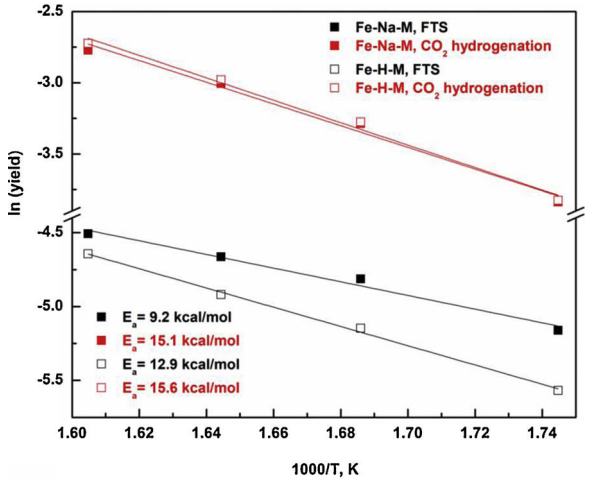

Fig. 8. Arrhenius plot of Fe-H-M and Fe-Na-M for FTS and CO_2 hydrogenation, with olefin and CO yield used to calculate the respective apparent activation energies. The detailed experimental procedure for these plots can be found in the Supplementary material.

studies using alkali metal promoters for RWGS [88–93]. The effect of increasing the Na loading is shown in Table S4, which results in monotonically decreasing CO_2 conversion, but the CO selectivity is relatively unchanged (~75%).

To further understand the difference in performance between the Fe-Na-M and Fe-H-M catalysts, apparent activation energies for FTS and CO_2 hydrogenation are calculated from the Arrhenius plots in Fig. 8, with the temperature profile and experimental procedure outlined in Fig. S9. As shown in Fig. 8 for FTS, Fe-Na-M has a lower E_a (9.2 kcal/mol) than Fe-H-M (12.9 kcal/mol), which is consistent with apparent activation barriers over Fe based catalysts [94–99]. For CO_2 hydrogenation, the activation barriers over Fe-Na-M (E_a = 15.1 kcal/mol) and Fe-H-M (E_a = 15.6 kcal/mol) are similar, which agree with other reported values for CO_2 hydrogenation catalysts [100–103]. Clearly in FTS, the addition of Na facilitates olefin production, which is observed by the decrease in apparent activation barrier. In CO_2 hydrogenation, the apparent activation barriers are similar, but the addition of Na results in an increase of selectivity to C_2-C_4 olefins and CO, providing additional evidence that Na promotes the production of desirable products.

The detailed performance of the Fe-based catalysts versus time on stream for CO_2 hydrogenation is shown in Fig. 9 and Fig. S10. For both catalysts, the CO_2 conversion is stable up to 12 h time-on-stream, however for Fe-H-M (Fig. 8a), the selectivity to CH_4 and C_2-C_4 hydrocarbons decrease, and the selectivity to CO increases with time. For Fe-Na-M, the CO selectivity increases to slightly above 80%, suggesting that Na improves the catalytic stability. This is a similar observation to FTS, where C_2-C_4 selectivity decreases over Fe-H-M, but remains stable over Fe-Na-M, which is likely because the short chain hydrocarbons react over the strong acid sites of H-ZSM-5, resulting in coke formation and decreased hydrocarbon production.

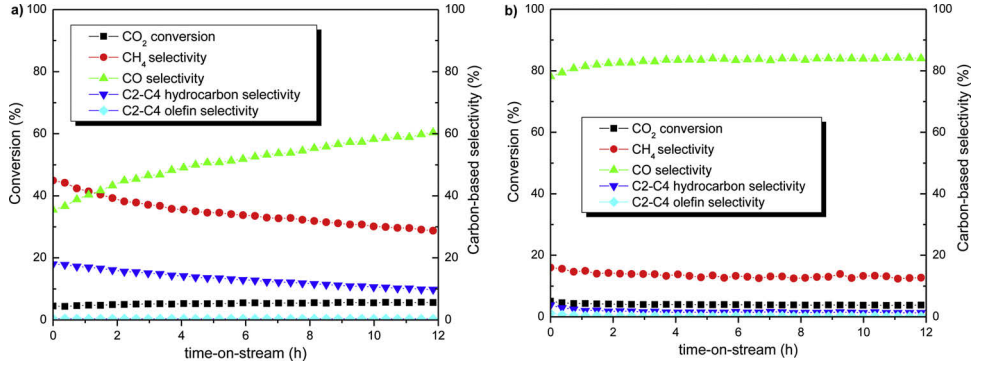

Fig. 9. Reactor performance versus time on stream for (a) Fe-H-M and (b) Fe-Na-M for CO_2 hydrogenation. Reaction conditions: CO_2:H_2 = 1:3, CO_2 (10 mL/min), H_2 (30 mL/min), and Ar (5 mL/min) as balance gas and internal standard; T = 335 °C, P = 300 psig, 200 mg catalyst, GHSV = 13500 mL h^{-1} g_{cat}^{-1}.

4. Conclusions

The effect of the ZSM-5 extra framework cation on FTS and CO_2 hydrogenation is evaluated over Fe-based catalysts. For FTS, Fe/Na-ZSM-5 results in improved catalytic stability and olefin selectivity over Fe/H-ZSM-5 because of an increase in surface basicity and greater extent of formation of the active Fe_5C_2 phase. The presence of the acidic zeolite, ZSM-5, may further crack the primary long-chain hydrocarbon products into the secondary olefin products. However, for CO_2 hydrogenation, RWGS becomes the dominant reaction over both Na- and H-form catalysts, and the Fe/Na-ZSM-5 shows higher selectivity toward CO than Fe/H-ZSM-5 from increased binding strength of CO_2. The results in this study show that the selectivity to the desired product, olefins for FTS and CO for RWGS, can be controlled by attenuating the acidic properties of the catalyst.

CRediT authorship contribution statement

Renjie Liu: Investigation, Writing - review & editing, Visualization. **Zhiqiang Ma:** Investigation, Writing - original draft, Visualization. **Jeffrey D. Sears:** Investigation, Visualization. **Mitchell Juneau:** Investigation. **Michael L. Neidig:** Supervision, Funding acquisition. **Marc D. Porosoff:** Conceptualization, Supervision, Project administration.

Declaration of Competing Interest

The authors declare that they have no known competing financial interests or personal relationships that could have appeared to influence the work reported in this paper.

Acknowledgements

RL, ZM, MJ and MDP would like to acknowledge support from the U.S. Department of Defense, Office of Naval Research, under Award No. N00173-18-P-1439. JDS and MLN would like to acknowledge a grant from the National Science Foundation (CHE-1954480 to MLN).

Appendix A. Supplementary data

Supplementary material related to this article can be found, in the online version, at doi:https://doi.org/10.1016/j.jcou.2020.101290.

References

[1] S. Posada-Pérez, P.J. Ramírez, J. Evans, F. Viñes, P. Liu, F. Illas, J.A. Rodriguez, Highly Active Au/δ-MoC and Cu/δ-MoC catalysts for the conversion of CO_2: the metal/C ratio as a key factor defining activity, selectivity, and stability, J. Am. Chem. Soc. 138 (2016) 8269–8278.
[2] M.D. Porosoff, B. Yan, J.G. Chen, Catalytic reduction of CO_2 by H_2 for synthesis of CO, methanol and hydrocarbons: challenges and opportunities, Energy Environ. Sci. 9 (2016) 62–73.
[3] G. Ji, Z. Yang, H. Zhang, Y. Zhao, B. Yu, Z. Ma, Z. Liu, Hierarchically mesoporous o-hydroxyazobenzene polymers: synthesis and their applications in CO2 capture and conversion, Angew. Chem. Int. Ed. 55 (2016) 9685–9689.
[4] Y. Cheng, J. Lin, K. Xu, H. Wang, X. Yao, Y. Pei, S. Yan, M. Qiao, B. Zong, Fischer–tropsch synthesis to lower olefins over potassium-promoted reduced graphene oxide supported iron catalysts, ACS Catal. 6 (2016) 389–399.
[5] V.V. Ordomsky, Y. Luo, B. Gu, A. Carvalho, P.A. Chernavskii, K. Cheng, A.Y. Khodakov, Soldering of iron catalysts for direct synthesis of light olefins from syngas under mild reaction conditions, ACS Catal. 7 (2017) 6445–6452.
[6] Z. Ma, M.D. Porosoff, Development of tandem catalysts for CO2 hydrogenation to Olefins, ACS Catal. 9 (2019) 2639–2656.
[7] A. Hwang, M. Kumar, J.D. Rimer, A. Bhan, Implications of methanol disproportionation on catalyst lifetime for methanol-to-olefins conversion by HSSZ-13, J. Catal. 346 (2017) 154–160.
[8] K.P. Kuhl, T. Hatsukade, E.R. Cave, D.N. Abram, J. Kibsgaard, T.F. Jaramillo, Electrocatalytic conversion of carbon dioxide to methane and methanol on transition metal surfaces, J. Am. Chem. Soc. 136 (2014) 14107–14113.
[9] F. Studt, I. Sharafutdinov, F. Abild-Pedersen, C.F. Elkjær, J.S. Hummelshøj, S. Dahl, I. Chorkendorff, J.K. Nørskov, Discovery of a Ni-Ga catalyst for carbon dioxide reduction to methanol, Nat. Chem. 6 (2014) 320–324.
[10] C.-S. Li, G. Melaet, W.T. Ralston, K. An, C. Brooks, Y. Ye, Y.-S. Liu, J. Zhu, J. Guo, S. Alayoglu, G.A. Somorjai, High-performance hybrid oxide catalyst of manganese and cobalt for low-pressure methanol synthesis, Nat. Commun. 6 (2015) 6538–6542.
[11] S. Kuld, M. Thorhauge, H. Falsig, C.F. Elkjær, S. Helveg, I. Chorkendorff, J. Sehested, Quantifying the promotion of Cu catalysts by ZnO for methanol synthesis, Science 352 (2016) 969–974.
[12] J. Zhong, J. Han, Y. Wei, S. Xu, Y. He, Y. Zheng, M. Ye, X. Guo, C. Song, Z. Liu, Increasing the selectivity to ethylene in the MTO reaction by enhancing diffusion limitation in the shell layer of SAPO-34 catalyst, Chem. Commun. 54 (2018) 3146–3149.
[13] W. Dai, C. Wang, M. Dyballa, G. Wu, N. Guan, L. Li, Z. Xie, M. Hunger, Understanding the early stages of the methanol-to-olefin conversion on H-SAPO-34, ACS Catal. 5 (2015) 317–326.
[14] W. Chen, I.A.W. Filot, R. Pestman, E.J.M. Hensen, Mechanism of cobalt-catalyzed CO hydrogenation: 2. fischer–tropsch synthesis, ACS Catal. (2017) 8061–8071.
[15] Y. Zhu, X. Pan, F. Jiao, J. Li, J. Yang, M. Ding, Y. Han, Z. Liu, X. Bao, Role of manganese oxide in syngas conversion to light olefins, ACS Catal. 7 (2017) 2800–2804.
[16] F. Jiao, X. Pan, K. Gong, Y. Chen, G. Li, X. Bao, Shape-selective zeolites promote ethylene formation from Syngas via a ketene intermediate, Angew. Chem. Int. Ed. 57 (2018) 4692–4696.
[17] Y. Yuan, S. Huang, H. Wang, Y. Wang, J. Wang, J. Lv, Z. Li, X. Ma, Monodisperse nano-Fe_3O_4 on α-Al_2O_3 catalysts for Fischer–Tropsch synthesis to lower olefins: promoter and size effects, ChemCatChem 9 (2017) 3144–3152.
[18] G. Yin, X. Yuan, X. Du, W. Zhao, Q. Bi, F. Huang, Efficient reduction of CO_2 to CO using cobalt–cobalt oxide core–shell catalysts, Chem. – A Eur. J. 24 (2018) 2157–2163.
[19] L. Zhong, F. Yu, Y. An, Y. Zhao, Y. Sun, Z. Li, T. Lin, Y. Lin, X. Qi, Y. Dai, L. Gu, J. Hu, S. Jin, Q. Shen, H. Wang, Cobalt carbide nanoprisms for direct production of lower olefins from syngas, Nature 538 (2016) 84–87.
[20] M. Juneau, M. Vonglis, J. Hartvigsen, L. Frost, D. Bayerl, M. Dixit, G. Mpourmpakis, J.R. Morse, J.W. Baldwin, H.D. Willauer, M.D. Porosoff, Assessing the viability of K-Mo2C for reverse water–gas shift scale-up: molecular to laboratory to pilot scale, Energy Environ. Sci. (2020).
[21] G. Zhan, H.C. Zeng, ZIF-67-derived nanoreactors for controlling product selectivity in CO_2 hydrogenation, ACS Catal. 7 (2017) 7509–7519.
[22] W. Wang, S. Wang, X. Ma, J. Gong, Recent advances in catalytic hydrogenation of carbon dioxide, Chem. Soc. Rev. 40 (2011) 3703–3727.
[23] S. Sartipi, K. Parashar, M.J. Valero-Romero, V.P. Santos, B. van der Linden, M. Makkee, F. Kapteijn, J. Gascon, Hierarchical H-ZSM-5-supported cobalt for the direct synthesis of gasoline-range hydrocarbons from syngas: advantages, limitations, and mechanistic insight, J. Catal. 305 (2013) 179–190.
[24] B.C. Sempuga, Y. Yao, CO_2 hydrogenation from a process synthesis perspective: setting up process targets, J. CO2 Util. 20 (2017) 34–42.
[25] Q. Zhang, J. Kang, Y. Wang, Development of novel catalysts for Fischer–Tropsch synthesis: tuning the product selectivity, ChemCatChem 2 (2010) 1030–1058.
[26] C. Xie, C. Chen, Y. Yu, J. Su, Y. Li, G.A. Somorjai, P. Yang, Tandem catalysis for CO_2 hydrogenation to C_2–C_4 hydrocarbons, Nano Lett. 17 (2017) 3798–3802.
[27] Y. Zhang, G. Jacobs, D.E. Sparks, M.E. Dry, B.H. Davis, CO and CO_2 hydrogenation study on supported cobalt Fischer–Tropsch synthesis catalysts, Catal. Today 71 (2002) 411–418.
[28] H.D. Willauer, R. Ananth, M.T. Olsen, D.M. Drab, D.R. Hardy, F.W. Williams, Modeling and kinetic analysis of CO2 hydrogenation using a Mn and K-promoted Fe catalyst in a fixed-bed reactor, J. CO2 Util. 3-4 (2013) 56–64.
[29] Z. Li, L. Zhong, F. Yu, Y. An, Y. Dai, Y. Yang, T. Lin, S. Li, H. Wang, P. Gao, Y. Sun, M. He, Effects of sodium on the catalytic performance of CoMn catalysts for Fischer–Tropsch to olefin reactions, ACS Catal. 7 (2017) 3622–3631.
[30] J. Lu, L. Yang, B. Xu, Q. Wu, D. Zhang, S. Yuan, Y. Zhai, X. Wang, Y. Fan, Z. Hu, Promotion effects of nitrogen doping into carbon nanotubes on supported iron Fischer–Tropsch catalysts for lower olefins, ACS Catal. 4 (2014) 613–621.
[31] A. Ramirez, A. Dutta Chowdhury, A. Dokania, P. Cnudde, M. Caglayan, I. Yarulina, E. Abou-Hamad, L. Gevers, S. Ould-Chikh, K. De Wispelaere, V. van Speybroeck, J. Gascon, Effect of zeolite topology and reactor configuration on the direct conversion of CO2 to light olefins and aromatics, ACS catalysis 9 (2019) 6320–6334.
[32] J. Wei, R. Yao, Q. Ge, Z. Wen, X. Ji, C. Fang, J. Zhang, H. Xu, J. Sun, Catalytic hydrogenation of CO_2 to isoparaffins over Fe-based multifunctional catalysts, ACS Catal. 8 (2018) 9958–9967.
[33] M.R. Gogate, R.J. Davis, Comparative study of CO and CO2 hydrogenation over supported Rh–Fe catalysts, Catal. Commun. 11 (2010) 901–906.
[34] R.W. Dorner, D.R. Hardy, F.W. Williams, H.D. Willauer, Heterogeneous catalytic CO2 conversion to value-added hydrocarbons, Energy Environ. Sci. 3 (2010) 884–890.
[35] W. Ning, N. Koizumi, M. Yamada, Researching fe catalyst suitable for CO2-containing syngas for Fischer－Tropsch synthesis, Energy Fuels 23 (2009) 4696–4700.
[36] J. Wei, Q. Ge, R. Yao, Z. Wen, C. Fang, L. Guo, H. Xu, J. Sun, Directly converting CO2 into a gasoline fuel, Nat. Commun. 8 (2017) 15174–15181.
[37] H.M. Torres Galvis, K.P. de Jong, Catalysts for production of lower olefins from synthesis gas: a review, ACS Catal. 3 (2013) 2130–2149.
[38] H. Mochizuki, T. Yokoi, H. Imai, R. Watanabe, S. Namba, J.N. Kondo, T. Tatsumi, Facile control of crystallite size of ZSM-5 catalyst for cracking of hexane, Micropor. Mesopor. Mater. 145 (2011) 165–171.
[39] T. Li, Z. Ma, F. Krumeich, A.J. Knorpp, A.B. Pinar, J.A. van Bokhoven, Properties modification of nano-sized hollow zeolite crystals by desilication, ChemNanoMat 4 (2018) 992–999.

[40] V.I. Pârvulescu, V. Pârvulescu, D. Macovei, L. Frunza, Hydrogenation of vinylbenzenes on Pd–Tm/Al2O3 and Tm/Al2O3 catalysts, J. Chem. Soc., Faraday Trans. 93 (1997) 1827–1835.

[41] S. Jiang, H. Zhang, Y. Yan, X. Zhang, Stability and deactivation of Fe-ZSM-5 zeolite catalyst for catalytic wet peroxide oxidation of phenol in a membrane reactor, RSC Adv. 5 (2015) 41269–41277.

[42] C. Wen, C. Wang, L. Chen, X. Zhang, Q. Liu, L. Ma, Effect of hierarchical ZSM-5 zeolite support on direct transformation from syngas to aromatics over the iron-based catalyst, Fuel 244 (2019) 492–498.

[43] M.M. Rafi, K.S.Z. Ahmed, K.P. Nazeer, D. Siva Kumar, M. Thamilselvan, Synthesis, characterization and magnetic properties of hematite (α-Fe2O3) nanoparticles on polysaccharide templates and their antibacterial activity, Applied Nanosci. 5 (2015) 515–520.

[44] J. Li, X. Cheng, C. Zhang, Q. Chang, J. Wang, X. Wang, Z. Lv, W. Dong, Y. Yang, Y. Li, Effect of alkalis on iron-based Fischer-Tropsch synthesis catalysts: Alkali-FeOx interaction, reduction, and catalytic performance, Appl. Catal. A: Gen. 528 (2016) 131–141.

[45] X. An, B.-s. Wu, H.-J. Wan, T.-Z. Li, Z.-C. Tao, H.-W. Xiang, Y.-W. Li, Comparative study of iron-based Fischer–Tropsch synthesis catalyst promoted with potassium or sodium, Catal. Commun. 8 (2007) 1957–1962.

[46] Z. Song, Q. Zhang, P. Ning, Y. Wang, Y. Duan, J. Wang, Z. Huang, Catalytic hydrolysis of HCN on ZSM-5 modified by Fe or Nb for HCN removal: surface species and performance, RSC Adv. 6 (2016) 111389–111397.

[47] M. Kuriyama, H. Tanaka, S.-i. Ito, T. Kubota, T. Miyao, S. Naito, K. Tomishige, K. Kunimori, Promoting mechanism of potassium in preferential CO oxidation on Pt/Al_2O_3, J. Catal. 252 (2007) 39–48.

[48] S.-H. Kang, J.W. Bae, P.S. Sai Prasad, K.-W. Jun, Fischer–Tropsch synthesis using zeolite-supported iron catalysts for the production of light hydrocarbons, Catal. Lett. 125 (2008) 264–270.

[49] A. Ramirez, A. Dutta Chowdhury, A. Dokania, P. Cnudde, M. Caglayan, I. Yarulina, E. Abou-Hamad, L. Gevers, S. Ould-Chikh, K. De Wispelaere, V. van Speybroeck, J. Gascon, Effect of zeolite topology and reactor configuration on the direct conversion of CO2 to light olefins and aromatics, ACS Catal. (2019) 6320–6334.

[50] Y. Xu, D. Liu, X. Liu, Conversion of syngas toward aromatics over hybrid Fe-based Fischer-Tropsch catalysts and HZSM-5 zeolites, Appl. Catal. A 552 (2018) 168–183.

[51] J. Xie, H.M. Torres Galvis, A.C.J. Koeken, A. Kirilin, A.I. Dugulan, M. Ruitenbeek, K.P. deJong, Size and promoter effects on stability of carbon-nanofiber-supported iron-based fischer–tropsch catalysts, ACS Catal. 6 (2016) 4017–4024.

[52] J. Xie, J. Yang, A.I. Dugulan, A. Holmen, D. Chen, K.P. de Jong, M.J. Louwerse, Size and promoter effects in supported iron Fischer–Tropsch catalysts: insights from experiment and theory, ACS Catal. 6 (2016) 3147–3157.

[53] P.A. Chernavskii, V.O. Kazak, G.V. Pankina, Y.D. Perfiliev, T. Li, M. Virginie, A.Y. Khodakov, Influence of copper and potassium on the structure and carbidisation of supported iron catalysts for Fischer-Tropsch synthesis, Catal. Sci. Technol. 7 (2017) 2325–2334.

[54] S. Abelló, D. Montané, Exploring iron-based multifunctional catalysts for Fischer–Tropsch synthesis: a review, ChemSusChem 4 (2011) 1538–1556.

[55] S.Z. Li, S. Krishnamoorthy, A.W. Li, G.D. Meitzner, E. Iglesia, Promoted iron-based catalysts for the Fischer-Tropsch synthesis: design, synthesis, site densities, and catalytic properties, J. Catal. 206 (2002) 202–217.

[56] H.M. Torres Galvis, J.H. Bitter, T. Davidian, M. Ruitenbeek, A.I. Dugulan, K.P. deJong, Iron particle size effects for direct production of lower olefins from synthesis gas, J. Am. Chem. Soc. 134 (2012) 16207–16215.

[57] H.M. Torres Galvis, J.H. Bitter, C.B. Khare, M. Ruitenbeek, A.I. Dugulan, K.P. deJong, Supported iron nanoparticles as catalysts for sustainable production of lower olefins, Science 335 (2012) 835–838.

[58] J.L. Weber, I. Dugulan, P. de Jongh, E.K.P. de Jong, Bifunctional catalysis for the conversion of synthesis gas to olefins and aromatics, ChemCatChem 10 (2017) 1107–1112.

[59] K.S. Park, J.H. Kim, S.H. Park, D.J. Moon, H.-S. Roh, C.-H. Chung, S.H. Um, J.-H. Choi, J.W. Bae, Direct activation of CH4 to oxygenates and unsaturated hydrocarbons using N2O on Fe-modified zeolites, J. Mol. Catal. A: Chem. 426 (2017) 130–140.

[60] J. Pérez-Ramírez, J.C. Groen, A. Brückner, M.S. Kumar, U. Bentrup, M.N. Debbagh, L.A. Villaescusa, Evolution of isomorphously substituted iron zeolites during activation: comparison of Fe-beta and Fe-ZSM-5, J. Catal. 232 (2005) 318–334.

[61] L. Rodríguez-González, F. Hermes, M. Bertmer, E. Rodríguez-Castellón, A. Jiménez-López, U. Simon, The acid properties of H-ZSM-5 as studied by NH3-TPD and 27Al-MAS-NMR spectroscopy, Appl. Catal. A: Gen. 328 (2007) 174–182.

[62] Z. Song, A. Takahashi, N. Mimura, T. Fujitani, Production of propylene from ethanol over ZSM-5 Zeolites, Catal. Lett. 131 (2009) 364–369.

[63] D.S. Lima, O.W. Perez-Lopez, Catalytic conversion of glycerol to olefins over Fe, Mo, and Nb catalysts supported on zeolite ZSM-5, Renew. Energy 136 (2019) 828–836.

[64] S.S.R. Putluru, A.D. Jensen, A. Riisager, R. Fehrmann, Alkali resistant Fe-zeolite catalysts for SCR of NO with NH3 in flue gases, Topics Catal. 54 (2011) 1286–1292.

[65] E. Yuan, G. Wu, W. Dai, N. Guan, L. Li, One-pot construction of Fe/ZSM-5 zeolites for the selective catalytic reduction of nitrogen oxides by ammonia, Catal. Sci. Technol. 7 (2017) 3036–3044.

[66] S. Scirè, R. Fiorenza, A. Gulino, A. Cristaldi, P.M. Riccobene, Selective oxidation of CO in H2-rich stream over ZSM5 zeolites supported Ru catalysts: An investigation on the role of the support and the Ru particle size, Appl. Catal. A: Gen. 520 (2016) 82–91.

[67] A.F.H. Wielers, A.J.H.M. Kock, C.E.C.A. Hop, J.W. Geus, A.M. van Der Kraan, The reduction behavior of silica-supported and alumina-supported iron catalysts: a Mössbauer and infrared spectroscopic study, J. Catal. 117 (1989) 1–18.

[68] J.B. Benziger, L.R. Larson, An infrared spectroscopy study of the adsorption of CO on Fe/MgO, J. Catal. 77 (1982) 550–553.

[69] W.W. Lonergan, D.G. Vlachos, J.G. Chen, Correlating extent of Pt–Ni bond formation with low-temperature hydrogenation of benzene and 1,3-butadiene over supported Pt/Ni bimetallic catalysts, J. Catal. 271 (2010) 239–250.

[70] J. Couble, D. Bianchi, Heats of adsorption of linear CO species adsorbed on reduced Fe/Al2O3 catalysts using the AEIR method in diffuse reflectance mode, Applied Catal. A: Gen. 409-410 (2011) 28–38.

[71] D. Song, J. Li, Effect of catalyst pore size on the catalytic performance of silica supported cobalt Fischer–Tropsch catalysts, J. Mol.Catal. A: Chem. 247 (2006) 206–212.

[72] U. Seip, M.C. Tsai, K. Christmann, J. Küppers, G. Ertl, Interaction of Co with an Fe (111) surface, Surf. Sci. 139 (1984) 29–42.

[73] M. Jiang, N. Koizumi, M. Yamada, Adsorption Properties of iron and Iron – Manganese catalysts investigated by in-situ diffuse reflectance FTIR spectroscopy, J. Phys. Chem. B 104 (2000) 7636–7643.

[74] M. Juneau, R. Liu, Y. Peng, A. Malge, Z. Ma, M.D. Porosoff, Characterization of metal-zeolite composite catalysts: determining the environment of the active phase, ChemCatChem 12 (2020) 1826–1852.

[75] P. Zhai, C. Xu, R. Gao, X. Liu, M. Li, W. Li, X. Fu, C. Jia, J. Xie, M. Zhao, X. Wang, Y.-W. Li, Q. Zhang, X.-D. Wen, D. Ma, Highly tunable selectivity for syngas-derived alkenes over zinc and sodium-modulated Fe5C2 catalyst, Angew. Chem. Int. Ed. 55 (2016) 9902–9907.

[76] E. Jiménez-Barrera, P. Bazin, C. Lopez-Cartes, F. Romero-Sarria, M. Daturi, J.A. Odriozola, CO/H2 adsorption on a Ru/Al2O3 model catalyst for Fischer Trospch: effect of water concentration on the surface species, Appl. Catal. B: Environ. 237 (2018) 986–995.

[77] P.B. Merrill, R.J. Madix, Site blocking by hydrogen: CO on clean and H-presaturated Fe(100), Surf. Sci. 271 (1992) 81–84.

[78] J.W. Magee, R.M. Palomino, M.G. White, Infrared spectroscopy investigation of Fe-promoted Rh catalysts supported on titania and ceria for co hydrogenation, Catal. Lett. 146 (2016) 1771–1779.

[79] A.I. McNab, A.J. McCue, D. Dionisi, J.A. Anderson, Quantification and qualification by in-situ FTIR of species formed on supported-cobalt catalysts during the Fischer-Tropsch reaction, J. Catal. 353 (2017) 286–294.

[80] H.M. Torres Galvis, A.C.J. Koeken, J.H. Bitter, T. Davidian, M. Ruitenbeek, A.I. Dugulan, K.P. deJong, Effects of sodium and sulfur on catalytic performance of supported iron catalysts for the Fischer–Tropsch synthesis of lower olefins, J. Catal. 303 (2013) 22–30.

[81] M. Casavola, J. Xie, J.D. Meeldijk, N.A. Krans, A. Goryachev, J.P. Hofmann, A.I. Dugulan, K.P. de Jong, Promoted iron nanocrystals obtained via ligand exchange as active and selective catalysts for synthesis gas conversion, ACS Catal. 7 (2017) 5121–5128.

[82] Q. Chang, C. Zhang, C. Liu, Y. Wei, A.V. Cheruvathur, A.I. Dugulan, J.W. Niemantsverdriet, X. Liu, Y. He, M. Qing, L. Zheng, Y. Yun, Y. Yang, Y. Li, Relationship between iron carbide phases (ε-Fe_2C, Fe_7C_3, and χ-Fe_5C_2) and catalytic performances of Fe/SiO_2 Fischer–Tropsch catalysts, ACS Catal. 8 (2018) 3304–3316.

[83] J.S. Martinez-Espin, M. Mortén, T.V.W. Janssens, S. Svelle, P. Beato, U. Olsbye, New insights into catalyst deactivation and product distribution of zeolites in the methanol-to-hydrocarbons (MTH) reaction with methanol and dimethyl ether feeds, Catal. Sci. Technol. 7 (2017) 2700–2716.

[84] J. Li, Y. Wei, G. Liu, Y. Qi, P. Tian, B. Li, Y. He, Z. Liu, Comparative study of MTO conversion over SAPO-34, H-ZSM-5 and H-ZSM-22: Correlating catalytic performance and reaction mechanism to zeolite topology, Catal. Today 171 (2011) 221–228.

[85] K. Lee, S. Lee, Y. Jun, M. Choi, Cooperative effects of zeolite mesoporosity and defect sites on the amount and location of coke formation and its consequence in deactivation, J. Catal. 347 (2017) 222–230.

[86] S. Müller, Y. Liu, M. Vishnuvarthan, X. Sun, A.C. van Veen, G.L. Haller, M. Sanchez-Sanchez, J.A. Lercher, Coke formation and deactivation pathways on H-ZSM-5 in the conversion of methanol to olefins, J. Catal. 325 (2015) 48–59.

[87] E. Rytter, A. Holmen, Perspectives on the effect of water in cobalt Fischer–Tropsch synthesis, ACS Catal. 7 (2017) 5321–5328.

[88] M.K. Gnanamani, H.H. Hamdeh, W.D. Shafer, S.D. Hopps, B.H. Davis, Hydrogenation of carbon dioxide over iron carbide prepared from alkali metal promoted iron oxalate, Appl. Catal. A: Gen. 564 (2018) 243–249.

[89] W. Xu, P.J. Ramírez, D. Stacchiola, J.L. Brito, J.A. Rodriguez, The carburization of transition metal molybdates (MxMoO4, M = Cu, Ni or Co) and the generation of highly active metal/carbide catalysts for CO2 hydrogenation, Catal. Lett. 145 (2015) 1365–1373.

[90] M.D. Porosoff, S. Kattel, W. Li, P. Liu, J.G. Chen, Identifying trends and descriptors for selective CO_2 conversion to CO over transition metal carbides, Chem. Commun. 51 (2015) 6988–6991.

[91] M.D. Porosoff, J.W. Baldwin, X. Peng, G. Mpourmpakis, H.D. Willauer, Potassium-promoted molybdenum carbide as a highly active and selective catalyst for CO2 conversion to CO, ChemSusChem 10 (2017) 2408–2415.

[92] E.V. Kondratenko, G. Mul, J. Baltrusaitis, G.O. Larrazabal, J. Perez-Ramirez, Status and perspectives of CO2 conversion into fuels and chemicals by catalytic, photocatalytic and electrocatalytic processes, Energy Environ. Sci. 6 (2013) 3112–3135.

[93] M.D. Porosoff, J.G. Chen, Trends in the catalytic reduction of CO_2 by hydrogen over supported monometallic and bimetallic catalysts, J. Catal. 301 (2013) 30–37.

[94] M. Ojeda, R. Nabar, A.U. Nilekar, A. Ishikawa, M. Mavrikakis, E. Iglesia, CO activation pathways and the mechanism of Fischer-Tropsch synthesis, J. Catal. 272

(2010) 287–297.
[95] G.T.K.K. Gunasooriya, A.P. van Bavel, H.P.C.E. Kuipers, M. Saeys, Key role of surface hydroxyl groups in C–O activation during Fischer–Tropsch synthesis, ACS Catal. 6 (2016) 3660–3664.
[96] K. Kondamudi Sonal, K.K. Pant, S. Upadhyayula, Synergistic effect of Fe–Co bimetallic catalyst on FTS and WGS activity in the Fischer–Tropsch process: a kinetic study, Ind. Eng. Chem. Res. 56 (2017) 4659–4671.
[97] M. Zhuo, K.F. Tan, A. Borgna, M. Saeys, Density functional theory study of the CO insertion mechanism for Fischer − Tropsch synthesis over Co catalysts, J. Phys. Chem. C 113 (2009) 8357–8365.
[98] O.R. Inderwildi, S.J. Jenkins, D.A. King, Fischer − Tropsch mechanism revisited: alternative pathways for the production of higher hydrocarbons from synthesis gas, J. Phys. Chem. C 112 (2008) 1305–1307.
[99] J. Cheng, P. Hu, P. Ellis, S. French, G. Kelly, C.M. Lok, A First-principles study of oxygenates on co surfaces in Fischer − Tropsch synthesis, J. Phys. Chem. C 112 (2008) 9464–9473.
[100] J. Dean, Y. Yang, N. Austin, G. Veser, G. Mpourmpakis, Designing Cu-based bimetallic nanoparticles for CO2 adsorption and activation, ChemSusChem 11 (2018) 1169–1178.
[101] X. Nie, H. Wang, M.J. Janik, Y. Chen, X. Guo, C. Song, Mechanistic insight into C–C coupling over Fe–Cu bimetallic catalysts in CO2 hydrogenation, J. Phys. Chem. C 121 (2017) 13164–13174.
[102] S. Kattel, P. Liu, J.G. Chen, Tuning selectivity of CO2 hydrogenation reactions at the metal/oxide interface, J. Am. Chem. Soc. 139 (2017) 9739–9754.
[103] Y.A. Daza, J.N. Kuhn, CO2 conversion by reverse water gas shift catalysis: comparison of catalysts, mechanisms and their consequences for CO2 conversion to liquid fuels, RSC Advances 6 (2016) 49675–49691.